Pinning-assisted outplane anisotropy in reverse stack FeCo/FePt intermetallic bilayers for controlled switching in spintronics

Garima Vashisht[1], Utkarsh Shashank[2], Surbhi Gupta[2], Rohit Medwal[3], C.L. Dong[4], C.L. Chen[5], K. Asokan[6], Y. Fukuma[2], S. Annapoorni[1,*]

[1]Department of Physics and Astrophysics, University of Delhi, Delhi-110007, India
[2]Department of Physics and Information Technology, Faculty of Computer Science and System Engineering, Kyushu Institute of Technology, Iizuka, Fukuoka 820-8502, Japan
[3]Natural Sciences and Science Education, National Institute of Education, Nanyang Technological University, Singapore 637616
[4]Department of Physics, Tamkang University, Tamsui, 251 Taiwan
[5]National Synchrotron Radiation Research Center, Hsinchu, 30076, Taiwan
[6]Material Science Division, Inter University Accelerator Centre, Aruna Asaf Ali Marg, New Delhi-110067, India

*Corresponding Author Email Id: annapoornis.phys@gmail.com

Abstract

Recent rapid progress in magnetic storage and processing devices require controlled characteristics of good thermal stability of magnetization (high coercive field) as well as low switching field which is possible by multilayer and nano-structuring. Here we study the implications of FeCo underlayer and overlayer on the static and dynamic magnetic properties of FeCo/FePt exchange spring system along with post annealing kinetics. Probing of FePt/FeCo/Si and FeCo/FePt/Si bilayers using high energy synchrotron X-Ray Diffraction by varying glancing angles unveiled structural variations at the interface, where FeCo is observed to inhibit the crystalline growth of FePt. The hysteresis loop establishes soft ferromagnetic in-plane behaviour and defect-driven hard ferromagnetic properties in the out-plane configuration. In addition to the out-plane hysteresis, the magnetization dynamics studied by Ferromagnetic Resonance depicts an out-plane magnetization component of FePt only in FeCo/FePt/Si. Next, X-Ray Absorption Spectroscopy (XAS) in the Fe, Co and Pt L-edge regions reveal dissimilar interface in the two series due to thermal agitation effects. XAS spectra at Fe and Co K-edges ensure similar local coordination of Co immaterial of stack order, contrary to altered local geometry of Fe observed in the two series ascribed to varied crystallinity of FePt. Such structures are useful for spin-wave assisted low field magnetization switching in highly coercive FePt by using exchange coupled soft FeCo.

Keywords

Exchange-spring; Anisotropy; Interface; Pinning; Gilbert damping; Charge transfer

Introduction

Rapidly emerging data storage and information processing technologies requires a quest for tailoring the magnetic properties of existing materials, popularly attained by nano-structuring like multilayers, superlattices, dots/arrays, core-shells etc. [1-4]. Over the decades, thin film

magnetic multilayers have been largely studied for their potential applications in wide range of permanent magnets [5,6], recording media [7,8,9], spintronic sensors and devices [10,11]. In particular, there have been several reports on FePt/FeNi [12], FePt/Fe [13], FePt/Fe_3Pt [14], FePt/FeCo [15] etc. exchange spring systems, prescribing their possible implementation in the above stated applications due to their large energy product or high coercivity (> 1 Tesla) offered by the system. Thanks to the intriguing properties of FePt that allows one to tune the anisotropy constant (K_u) of system as required, say K_u varying from 10^5 J/m^3 to 7×10^6 J/m^3 [16] corresponding to different phases that exist in system. The magnetic properties in FePt-based system strongly depends on the structural ordering of FePt [17], which in-turn is governed by various factors such as deposition conditions [18], substrate lattice matching [19], growth dynamics on buffer layer [20,21], post-annealing kinetics [22,23], doping induced chemical pressure [24,25], capping layer induced interface anisotropy [26] etc. However, the naturally high magneto-crystalline anisotropy in $L1_0$-FePt results in large coercivity which may surpass the fields of current writing heads [15]. Therefore, enormous efforts have been made to reduce the switching field and anisotropy in the FePt-based exchange spring media by manipulating the strongly coupled soft/hard magnetic interface [14,27]. Gu et al. reported the variation in energy product of FePt/Fe exchange spring system as a function of the thickness of Fe layer and obtained maximum energy product of 16 MGOe for FePt(203.4Å)/Fe(81.4Å) [28]. They correlated the experimental coercivities at different thickness of Fe with the structural transformations of FePt after annealing at 500 ˚C and 600 ˚C and observed that the degree of order in FePt decreases as the thickness of Fe is increased beyond 108.5 Å. Goll et al. suggested specially designed FePt/Fe graded interface for fine tuning of coercivity in the exchange spring system stating a decrease in coercivity of 0.22 T in graded interface of FePt/Fe as compared to the sharp interface which amounts to 1.24 T coercivity [29]. FeCo/FePt multilayers are the most interesting subject of research in magnetism offering unique properties of large saturation magnetization along with high coercivity, without compromising with the thermal stability [30]. Giannopoulos et al. reported a high energy product of 50 MGOe in FePt(5ML)/FeCo(5ML) with its decreasing value for increased monolayers (ML) of FeCo [30]. In our earlier study, we reported a high energy product of 49 MGOe in $L1_0$-FePt/FeCo system and investigated the exchange coupling between the two layers by dM/dH curve, recoil curves and micromagnetic simulations [31]. The observation of polycrystalline $L1_0$-FePt or (001) oriented $L1_0$-FePt and reducing the naturally high magnetocrystalline anisotropy energy has been largely evidenced. It is further interesting to investigate the means of reducing the ordering in FePt at elevated

temperatures, which would subsequently tune the anisotropy of the system. FeCo has an appropriate lattice parameter to alter the growth kinetics of FePt and also possess large saturation magnetization of 2.4 T [32,33]. Such properties of FeCo can be used to engineer the magnetic properties of exchange spring media. Wang et al. reported an induced tetragonality in FeCo films when deposited over (001) oriented FePt films, which enhanced the out of plane anisotropy of the system [15]. Guan et al. identified that the perpendicular magnetic anisotropy in MgO/FeCo/A1-FePt films (7.5×10^6 ergs/cm^3) originates from the strained interface [34]. However, firm experimental evidences to correlate the structural and magnetic aspects of polycrystalline FePt films when deposited over polycrystalline FeCo were not reported by them.

The present study focuses on an effective pathway to modify the anisotropy of FePt/FeCo multilayers via defect-mediated domain wall propagation. We study the effect of inversing the stack order of FeCo/FePt bilayers over oxidized Si substrate before and after providing thermal treatment. The layered structure of FeCo/FePt/Si and FePt/FeCo/Si was probed at different depths to identify any probable strain developed at the interface. In contrast to the high energy product generally attained in the FeCo/FePt multilayers, we demonstrate pinning-dominated coercivity mechanism in FeCo/FePt bilayers. Unlike ion beam modifications for creating local defects, here the defects are created inevitably due to the interface of two layers without disturbing the crystallinity of the layers. The effect of different interfaces developed in FeCo/FePt/Si and FePt/FeCo/Si on the magnetization dynamics of the system are studied by exciting ferromagnetic resonance. After establishing the magnetic properties and magnetization reversal mechanism, the detailed investigation of electronic interactions between the atoms at the interface is studied by X-Ray Absorption spectroscopy (XAS) and is subsequently related to the observed magnetic properties.

Experimental Details

FeCo/FePt multilayers were deposited on SiO_2 coated Si substrates oriented along <100> plane using two target RF magnetron sputtering. The base pressure of the sputtering chamber was maintained at 4×10^{-6} Torr and a high Ar pressure of 6×10^{-2} Torr was used during the sputtering. Commercially purchased equi-atomic $Fe_{50}Co_{50}$ and $Fe_{50}Pt_{50}$ alloy targets of 99.9% purity were used for the deposition. The surfaces of both the targets were cleaned by sputtering initially for 10 minutes before depositing the films onto the substrates. Thereafter, the FeCo/FePt multilayers were deposited on the substrates by alternatively turning on the power supply for FeCo and FePt targets. A high power of 200 W was used for the deposition

of FeCo films, while RF power of 60 W was used for FePt films. The thickness was controlled by varying the time of deposition. Two sets of samples were deposited: (a) the FeCo films on oxidized Si substrate followed by the deposition of FePt thin films over FeCo and (b) the FePt films on oxidized Si substrate followed by FeCo thin films over FePt. The films were annealed at 500 ˚C for 5 hours in a reducing atmosphere of Ar (95%) + H_2 (5%) using a microprocessor controlled tubular furnace so as to enhance the crystallinity. Rutherford Backscattering Spectroscopy (RBS) was performed to estimate the film thickness and chemical composition of each layer along the depth of samples. He^{2+} ions with 2 MeV energy are incident on the samples and the yield of backscattered ions is recorded as a function of energy. The ~~thickness~~ depth profile of samples was estimated by fitting the RBS spectra ~~obtained from the Rutherford Backscattering Spectroscopy (RBS)~~ using RUMP software (fig. S1). Table 1 lists the four set of films that are investigated in this study and their thicknesses.

Table 1: List of multilayers to be compared

Sample Details	Thermal Treatment	Long Name	Short Name
FePt(12.6nm)/FeCo(27nm)/Substrate	Pristine	FePt/FeCo/Si_As	P_As
FePt(12.6nm)/FeCo(27nm)/Substrate	Annealed at 500 ˚C	FePt/FeCo/Si_500	P_500
FeCo(28nm)/FePt(12.6nm)/Substrate	Pristine	FeCo/FePt/Si_As	C_As
FeCo(28nm)/FePt(12.6nm)/Substrate	Annealed at 500 ˚C	FeCo/FePt/Si_500	C_500

The surface morphology of the films was examined by Field Emission Scanning Electron Microscope (FESEM, Mira3 TESCAN). The structural aspects of the films were studied by Synchrotron X-Ray Diffraction (XRD) measurements, performed using 13keV energy in MCX beamline, Elettra Sinchrotrone facility, Italy [35]. The diffraction spectra were measured in glancing incidence mode fixing the glancing angle at 0.5˚. The diffraction spectra were also collected for varying glancing angles in order to investigate any strain developed at the interface of two layers. The bulk magnetic properties were measured using a Microsense EV-9 Vibrating Sample Magnetometer (VSM). The hysteresis loops were recorded at room temperature by applying the magnetic field both parallel and perpendicular to the film plane. The angular variation of coercivity was also recorded in order to study the domain wall propagation mechanism. The in-plane ferromagnetic resonance (FMR) measurements were performed in field-sweep mode using a Vector Network Analyser (VNA); the uniform FMR resonance mode was observed in the presence of the varying magnetic field at a fixed frequency, fulfilling the resonant condition for bilayer samples. All samples were placed over co-planar waveguide in flip-chip configuration to excite FMR. The

local electronic structure of the films was studied by XAS carried out at National Synchrotron Radiation Research Center (NSRRC), Taiwan. XAS of Fe and Co L-edges were performed at TLS BL20A1 in a vacuum chamber with a base pressure better than 1 x 10^{-9} torr in total electron yield (TEY) mode, aligning the film surface normal to the incident beam. The XAS at Pt L-edge and Fe/Co K-edge were collected in the fluorescence mode at TLS BL17C1.

Results and Discussions

The surface morphology of all the as prepared and annealed bilayers is presented in fig. S2 of supplementary material. The FESEM images of as prepared samples illustrate uniform granular structure with average grain size 14 nm and 23 nm in FePt/FeCo/Si_As and FeCo/FePt/Si_As respectively. After annealing at 500 ˚C, nanoparticle coalescence takes place. For FePt/FeCo/Si_500, the agglomeration of grains results in homogeneous distribution of irregular shaped grains over the substrate. While for FeCo/FePt/Si_500, spherical shaped grains with size ~34 nm are observed. Figure 1 shows the synchrotron XRD spectra of all the as prepared and annealed samples measured at 0.5˚ glancing angle. The XRD pattern of all the samples reveals that FeCo grows in BCC phase with lattice parameter 2.852 Å, 2.860 Å, 2.873 Å and 2.858 Å for P_As, P_500, C_As and C_500 multilayers respectively. Both the series show the formation of A1 phase of FePt in as prepared as well as annealed samples having lattice parameter 3.776 Å, 3.703 Å, 3.822 Å and 3.711 Å in P_As, P_500, C_As and C_500 respectively. The crystallinity of BCC FeCo and FePt in its A1 phase increases after annealing. No signatures of the superlattice peaks are evidenced. However, the diffraction peaks corresponding to the planes (002) and (201) begins to emerge indicating the initiation of FePt into $L1_0$ phase after annealing. Additional peaks corresponding to the oxides of iron and cobalt are also observed due to the surface oxidation in all the samples.

The nature of layered structures of FeCo and FePt along with their oxides was studied by varying the angle of incidence (θ) from 0.2˚ to 0.6˚ and collecting the diffraction spectra corresponding to the most intense peaks of FeCo and FePt. Figure 1 (b) and (c) shows the diffraction pattern near to (111) plane of FePt and (110) plane of FeCo at different θ for the annealed samples FePt/FeCo/Si_500 (fig. 1(b)) and FeCo/FePt/Si_500 (fig. 1(c)).

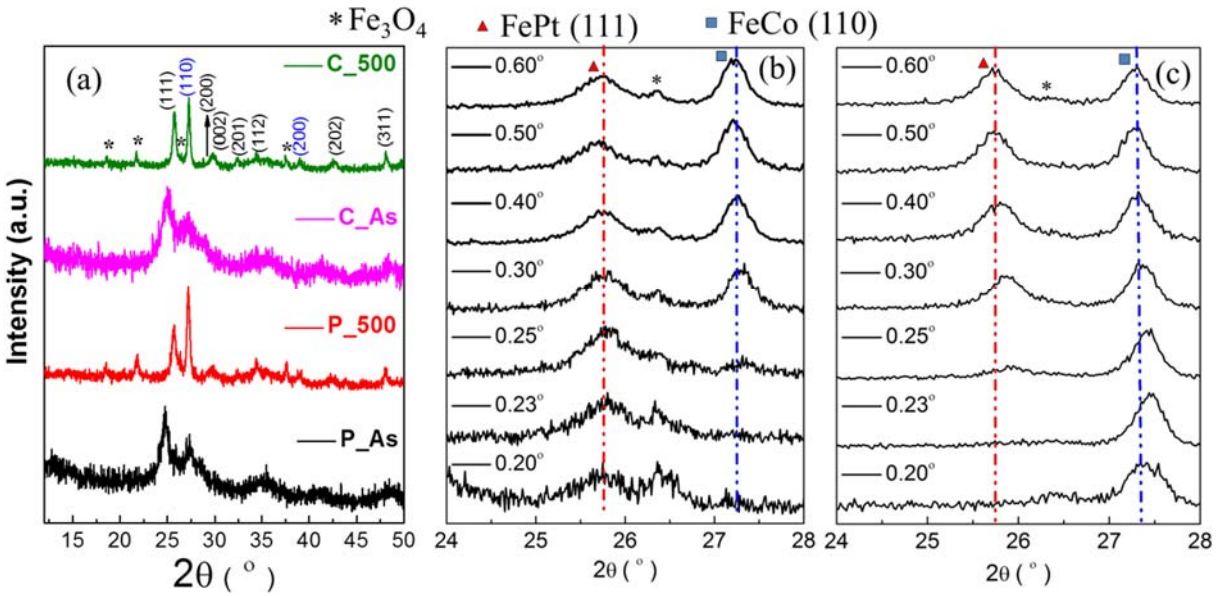

Figure 1. XRD spectra at 13 keV for (a) all bilayered samples (The (hkl) planes labelled in black corresponds to those of FePt and the ones in blue are for FeCo); XRD at different glancing angles for (b) P_500 and (c) C_500.

For sample P_500, at lower glancing angle of 0.2˚, the peak corresponding to (004) plane of Fe_3O_4 is the most intense followed by smaller peak of (111) plane of FePt. FeCo could not be observed at such lower θ since the X-Rays could not penetrate into the FeCo layer. This shows the presence of oxides on the surface of film. As θ is increased to 0.25˚, most intense (110) plane of FeCo begins to emerge. Further increasing the glancing angle to 0.30˚, (111) peak of FePt and (110) peak of FeCo are clearly visible. On increasing the glancing angle further, it is observed that the intensity of FeCo peak increases along with a slight shift in the 2θ values towards lower angle, while no significant shift is found for FePt. As a result, the lattice parameter of FeCo changes from 2.858 Å at θ = 0.30˚ to 2.860 Å at θ = 0.4˚ - 0.6˚ when it is probed deeper, indicating a slight compression in the unit cell for FeCo layer at the interface. On the other hand, for sample C_500, only a slight surface oxidation is observed as evidenced by minor hump at 26.48˚ and an intense peak of (110) plane of FeCo at lower glancing angle of θ = 0.2˚. The diffraction peak corresponding to (111) plane of FePt emerges after increasing the glancing angle to 0.25˚. In this case, a shift in the 2θ values towards the lower angle is observed both for FeCo as well as FePt when the X-Rays penetrate through the interface of two layers. The lattice parameter of FeCo on the surface was estimated to be 2.844 Å using the diffraction pattern obtained at 0.2˚. The lattice parameter of FeCo remains unchanged till FeCo layer comes in contact with FePt, where it was calculated as 2.858 Å using the diffraction pattern at 0.30˚ when the diffraction peak corresponding to (111) plane of FePt could be observed. Similarly, the lattice parameter of FePt changes from 3.686 Å to

3.711 Å on progressing from interface with FeCo to the interface with substrate. These angular dependent X-Ray diffraction measurements clearly depict dissimilarity in the interface formation between the two layers in FePt/FeCo/Si_500 and FeCo/FePt/Si_500. While for FePt/FeCo/Si_500, the variation in the lattice parameters of FeCo and FePt is negligible throughout the interface as well as bulk; for FeCo/FePt/Si_500, a strained interface is observed between the two layers as a consequence of expansion in FeCo lattice and compression in FePt unit cell. Therefore, these angular dependent X-ray measurements clearly reveal that the presence of FeCo plays a great role in the growth and phase formation of FePt.

In order to distinguish the role of FeCo and FePt layer on influencing the crystallinity of each other, the crystallite size of FeCo and FePt in all the samples was estimated by the Scherrer's formula using the most intense peaks of FeCo and FePt. The crystallite size of FeCo in the as prepared samples is 7 nm and 4 nm for P_As and C_As respectively. The crystallite size of FeCo increases to 17 nm for both P_500 and C_500 after annealing. For FePt, the crystallite size of 4 nm is observed for P_As and C_As. After annealing, the crystallite size of FePt increases to 10 nm when it is deposited over FeCo. On the other hand, it increases to 17 nm after annealing when it is grown over the oxidized Si substrate. This suggests underlayer FeCo inhibits the crystalline growth of FePt over it, while no such growth inhibition is observed for FeCo as an influence of FePt underlayer or overlayer. The effect of this inhibited growth of FePt on the magnetic properties of the system was observed using Vibrating Sample Magnetometer.

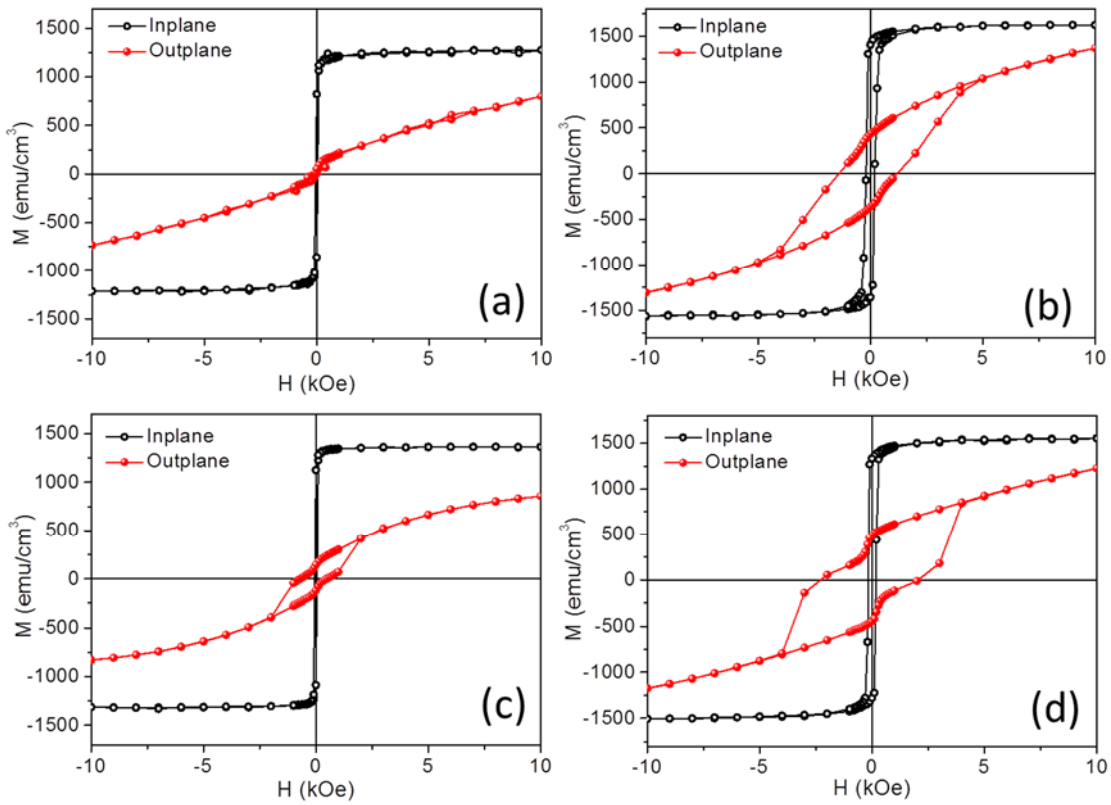

Figure 2. M-H curves at room temperature for (a) P_As, (b) P_500, (c) C_As and (d) C_500.

The room temperature magnetic properties are tested by recording the M-H curves in the in-plane and out-plane configurations for all the bilayers as well as the individual layers of FeCo and FePt on Si substrate. The M-H curves for individual layers of FeCo and FePt are shown in the supplemental material fig. S3 and the M-H curves for all bilayers are shown in fig. 2. ~~Figure 2 shows M-H curves at room temperature both in the in-plane and out-plane configurations for all the bilayers.~~ All the hysteresis loops saturates at a lower field of 1 kOe when the magnetic field is applied parallel to the film plane as compared to the out-plane configuration where the M-H curves do not saturate even upto a high field of 1 Tesla. This suggests that the easy axis in all the samples is oriented along the plane of the film. Single layer FeCo film shows high saturation magnetization (M_s) with soft ferromagnetic behaviour in both configurations for as prepared as well as annealed FeCo films (see figure S3(a) and (b) in supplemental material). The as prepared FePt thin film also shows low coercivity (H_c) of 130 Oe and 190 Oe in the in-plane and out-plane configuration respectively (fig. S3(c)). However, H_c rises to 1530 and 710 Oe in the in-plane and out-plane configuration respectively for FePt thin films after annealing as shown in fig. S3(d). For the bilayers, both the as prepared samples show a low ~~coercivity (H_c)~~ H_c of 48 Oe in the in-plane configuration (fig. 2(a) and (c)). When hysteresis loop is recorded while applying the magnetic field

perpendicular to the film plane, H_c remains the same for P_As (fig. 2(a)). However, when FeCo is deposited over FePt polycrystalline film, H_c increases to 685 Oe in the out-plane configuration for C_As (fig. 2(c)). When both the series are annealed at 500 ˚C, the in-plane H_c increases to 200 Oe and 170 Oe for sample P_500 (fig. 2(b)) and C_500 (fig. 2(d)) respectively. ~~The value of anisotropy constant (K) deduced from the in-plane M-H loops using the relation $K = \frac{H_c \times M_s}{2}$ (where M_s is the saturation magnetization) was calculated to be 2.7×10^4 J/m^3, 1.6×10^5 J/m^3, 4.9×10^4 J/m^3 and 2.4×10^5 J/m^3 for P_As, P_500, C_As and C_500. A clear increase in anisotropy constant is observed after annealing both the series.~~ A drastic increase in the coercivity is observed for both the series after annealing when magnetic field was applied perpendicular to the plane of film. The coercivity in out-plane configuration increases to 1402 Oe and 2272 Oe for P_500 and C_500 respectively. It is clear that the increase in ~~coercivity~~ H_c is more for the case where FePt is grown over the Si substrate. This enhanced coercivity observed only in the out-plane configuration is indicative of the presence of some second phase magnetic or non-magnetic inclusions acting as pinning sites. In our earlier study, we reported a large energy product of 47 MG-Oe for FeCo(x:6 nm, 12 nm)/FePt(27 nm)/Si system [31]. The pinning effects could not be observed for this thickness of FePt and FeCo. On decreasing the thickness of FePt to 12.6 nm, results in its varied ordering kinetics [36]. Therefore, more energy is required for the phase transformation of FePt and hence annealing at 500 ˚C is not sufficient to convert FePt into its $L1_0$ phase. Additionally, increasing the annealing temperature beyond 500 ˚C would result in the distorted interface between the two layers and diffusion of two layers into each other (see supplemental fig. S4). Therefore, the annealing temperature is restricted to 500 ˚C. Hence, it can be concluded that different thickness of FePt gives large variation in magnetic properties depending on the material over which it is deposited. The effective anisotropy constant (K_{eff}) is calculated by means of the area enclosed by in-plane and out-plane hysteresis loops using the following relation [37]:

$$K_{eff} = K_{out} - K_{in} = \int_{0\_Out}^{M_s} HdM - \int_{0\_In}^{M_s} HdM \quad (1)$$

Here H is the applied field and M is the magnetization. The obtained values of K_{eff} for all the samples along with other parameters deduced from the hysteresis curves are summarized in table 2. It could be seen that K_{eff} increases after annealing all the individual layers as well as the bilayer samples which can be ascribed to the grain growth after annealing [38]. At this point, it is important to note that the in-plane H_c for single layer FePt is more than that of any

of the bilayers. This clearly shows that the presence of FeCo as an underlayer or overlayer in FeCo/FePt system greatly suppresses the coercivity of system by inhibiting the crystalline growth of FePt. In addition, the K_{eff} values for the bilayers are greater than that of single layer films suggesting an enhanced anisotropy due to the interface of FeCo/FePt layers.

The difference in the coercivity observed for both the series could be attributed to strained interface of FeCo/FePt/Si_500. The lattice mismatch of two layers at the interface of FePt/FeCo/Si_500 is higher as compared to FeCo/FePt/Si_500 as demonstrated from glancing angle dependent synchrotron XRD. Large lattice misfit at the interface do not support enhancement in the coercivity to a large extent as compared to inhomogeneities created by the interface with lesser lattice mismatch [39]. Hence, large coercivity enhancement in FeCo/FePt/Si_500 in the outplane configuration as compared to FePt/FeCo/Si_500 may be interpreted by lesser lattice mismatch between FeCo and FePt in this series as compared to the other. Along with the increased coercivity, FeCo/FePt/Si series also show two-step hysteresis loop (fig. 2(c) and (d)). The appearance of shoulder in the M-H loop at ~ 0 Oe field signifies the uncoupled hard and soft ferromagnetic phase. In the present case, the in-plane hysteresis loop establishes soft ferromagnetic behaviour with single loop in all the bilayered samples. Therefore, the appearance of shoulder in the out of plane configuration of FeCo/FePt/Si series could be explained as a manifestation of the perpendicular component of magnetization in either of the layers or at interface, which remains uncoupled with the spins having easy axis oriented towards the film plane. The origin of perpendicular anisotropy in these bilayered samples is studied using FMR measurements and is discussed in the later section.

Table 2. Parameters deduced from M-H loops for individual layers and bilayers.

Sample	**M_s (emu/cm^3)**	**H_c:Inplane (Oe)**	**H_c:Out-plane (Oe)**	**K_{eff} ($\times 10^4$) (J/m^3)**
FeCo_As	1120	41	116	0.6
FeCo_500	1724	80	280	13.0
FePt_As	760	130	190	2.2
FePt_500	990	1530	710	26.0
P_As	1270	48	48	0.7
P_500	1600	200	1402	37.0
C_As	1364	48	685	4.6
C_500	1550	170	2272	38.0

The mechanism of domain wall propagation in FeCo/FePt bilayers and the effect of reverse stacking are understood by recording angular variation of coercivity. The angular variation of absolute values of coercivity for P_500 and C_500, shown in fig. 3(a), represents a sinusoidal

behaviour. The scaled coercivity as a function of angle between the applied magnetic field and film plane is shown in fig. 3(b). The dotted lines show theoretical fit using modified Kondorsky model and Stoner Wohlfarth (SW) Model [40, 41]. Figure 3(b) demonstrates that the coercivity mechanism follows modified Kondorsky model. This indicates the magnetization reversal occurring through domain wall unpinning due to defects in a system with uniaxial anisotropy. These defects originate from the interface of FeCo and FePt layers in both the series, which restricts the motion of domain wall with reversing field.

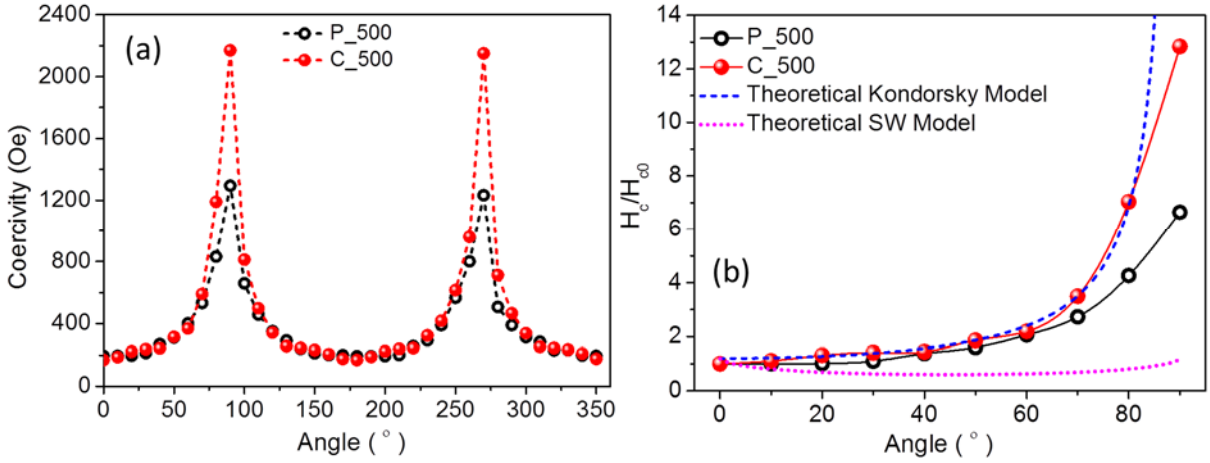

Figure 3. Angular variation of coercivity for P_500 and C_500 varying the polar angle from (a) 0˚ to 360˚ and (b) Magnified region from 0˚ to 90˚ with theoretical SW and Kondorsky Model.

Next, to understand the magnetization dynamics of both the as prepared bilayer samples, FMR spectra in the reflectance mode -S_{11} was recorded and is shown in figure 4. The varying external magnetic field is applied in the direction, parallel to the film plane during measurement. Figure 4(a) shows the FMR spectra for sample P_As with single peak. For the sample C_As, two distinguishable absorption peaks are observed (see figure 4(b)). The emergence of two peaks above 7 GHz suggests the presence of two different magnetic phases with distinct effective magnetization value attributed to strong exchange effect in P_As as compared to C_As. At low frequencies of 5 GHz and 6 GHz, the resonant field of magnetization precession of both the ferromagnets are very close resulting in the merged single peak. The recorded FMR was fitted with Lorentzian symmetric and anti-symmetric component to estimate the spectral linewidth (ΔH) and resonant field H_0 [42]. To estimate the effective magnetization of both the samples (P_As and C_As), the resonance field as a function of excitation frequencies were fitted with Kittle equation, $f = \gamma\mu_0\sqrt{H_0(H_0 + 4\pi M_{eff})}$, where f is the frequency, γ is the gyromagnetic ratio and M_{eff} is the effective magnetization (fig. 4(c)). For P_As, the $4\pi M_{eff}$ is estimated to be 1524 mT where,

single resonant peak is observed. A linear increase in the ΔH with f is observed. From the slope of linear frequency dependence, the Gilbert damping parameter α using $\Delta H = \Delta H_0 + \frac{2\pi}{\gamma}\alpha f$ is estimated where ΔH_0 is the inhomogeneous line broadening (fig. 4(e)). The value of α is estimated to be 0.041 for P_As. Higher damping factor may be attributed to intrinsic high damping factor of FePt (0.03) and interlayer exchange coupling [42]. For the sample C_As, two different M_{eff} values have been estimated considering two distinct resonant peaks for FMR spectra obtained at 9 GHz and above. The estimated $4\pi M_{eff}$ were 1842 mT and 845 mT. The former value of M_{eff} is close to the saturation magnetization of FeCo, while the latter value is less than that of A1 FePt. The reduced value of M_{eff} for A1 FePt, can be attributed to the presence of out-plane anisotropy in FePt ($K_\perp$), in addition with the in-plane component of magnetization, since $4\pi M_{eff} = 4\pi M_s - K_\perp$ [43, 44]. This is also apparent from the double phase hysteresis loop in the out of plane configuration for FeCo/FePt/Si series. The respective α for FeCo and FePt were estimated to be 0.014 and 0.027. The value of α for FePt matches well with reported value [42]. The variation in the damping factors is due the presence of the magnetostatic exchange interaction present in the system.

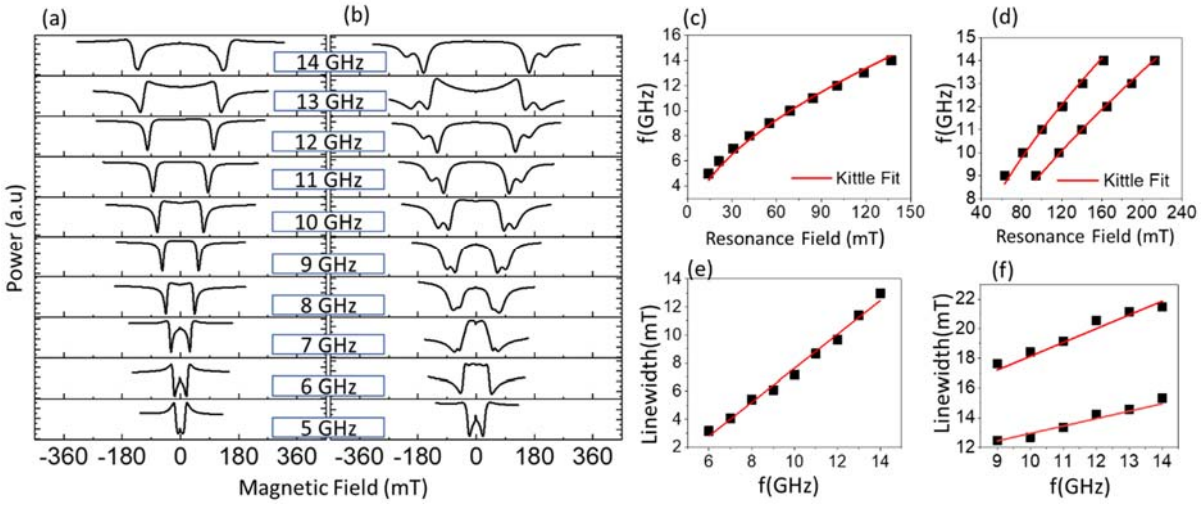

Figure 4. FMR spectra obtained in the broad frequency range of 5 GHz – 15 GHz for (a) P_As (b) C_As; Kittel fitting of (c) P_As (d) C_As; linear fitting of linewidth with frequency for (e) P_As (f) C_As.

XAS was used to study the local electronic structures around Fe, Co and Pt in the modified interface as a consequence of inversing the order of FeCo/FePt stacks and annealing. Figure 5 presents the Fe and Co L-edge spectra for all the as prepared and annealed samples. The XANES data is processed by subtracting the spectral background and normalizing the intensities to the post L_2-edge features. The L-edge spectra of Fe and Co results from electron transitions from $2p_{3/2}$ and $2p_{1/2}$ levels to unoccupied 3d levels, referred as L_3 and L_2 edges

348 respectively. The spectral features are influenced by crystal field interactions, Coulombic
349 repulsions, spin-orbit coupling, valence state, core-hole effects etc. [45,46].
350 In all the bilayered samples, L_3 and L_2 edges of Fe are nearly 13.3 eV apart, which depicts the
351 spin-orbit splitting of 13.3 eV, in well correspondence to literature value [47]. However, the
352 spectral features at $L_{3,2}$ edges of Fe presents multiplet structures in all the samples which
353 provides an indication of the surface oxidation of Fe. This is in conformity with the
354 synchrotron XRD measurements showing the diffraction peaks corresponding to Fe_3O_4. On
355 the other hand, the spectrum corresponding to $L_{3,2}$ edge of Co shows single, sharp and
356 asymmetric absorption peaks which resembles metallic Co^0 valence state. This is in
357 accordance with earlier reports stating that Co offers large resistance to oxidation as
358 compared to Fe [48]. The L_3 and L_2 edges of Co in all four samples occur at 776 eV and
359 791.6 eV respectively which are ~15.6 eV distant, consistent with the literature [49]. Since
360 transition metal (TM) L-edge requires only lower photon energy than TM K-edge, the
361 information associated with the surface can be presented in the soft X-ray absorption
362 spectrum. The increase in the oxidation state causes the multiple scattering factors of the 3d
363 orbital as an increase in the oxygen ligand hole density, which increases the orbital
364 hybridization phenomenon. In other words, the oxidation of the transition metal is observed
365 to increase hybridization that reflects the Fe/Co 3d and oxygen 2p energy level change. Due
366 to the increased covalency, the FWHM is indirectly proportional to this orbital hybridization,
367 the TM L-edge feature of oxides would reveal much broader FWHM than the metal (alloy)
368 [50,51]. A decrease in the broadening or FWHM of Fe and Co L_3-edges after annealing is
369 observed in both the series. This shows that Fe and Co exists as a mixture of metallic Fe^0, Co^0
370 as well as higher order valence states. The higher valence state essentially occurs due to the
371 surface oxidation of films especially in the as prepared samples, which gets reduced after
372 thermal annealing in $Ar+H_2$ atmosphere. A closer look to the valence state of Fe and Co will
373 be made later in the corresponding K-edge analysis.
374

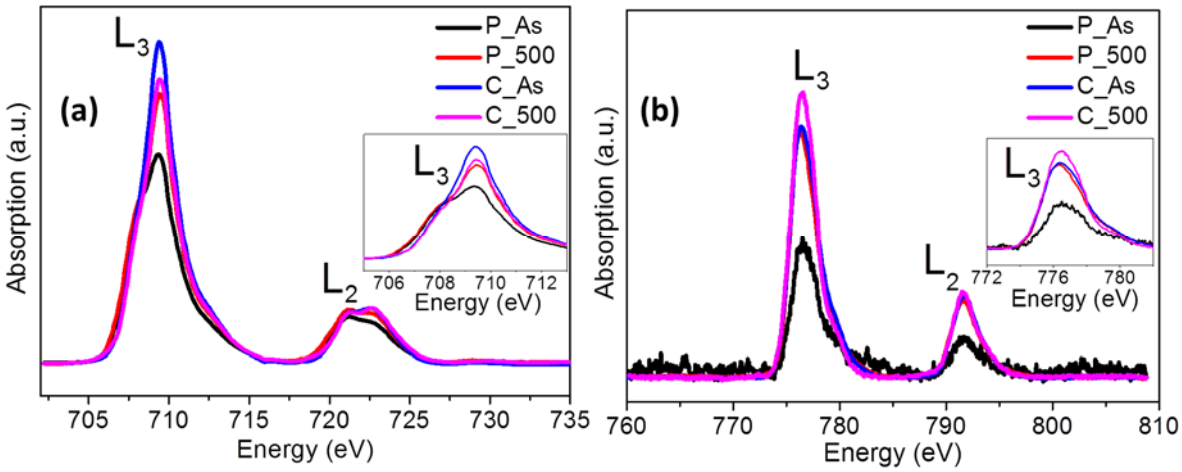

Figure 5.(a) Fe L-edge and (b) Co L-edge for all the samples. Inset shows magnified view of L_3 edges of Fe and Co. Note that the intensity changes after annealing.

Comparing the maximum intensities in the L_3-edge of Fe and Co provides information regarding the unoccupied 3d-orbitals in the ground state. The magnified L_3-edges of Fe and Co given in the inset of fig. 5(a) and (b) respectively, show that the intensity of absorption is the least for P_As at both Fe and Co L_3 edges. The intensity increases after annealing which signifies that the number of vacant 3d-orbitals in both Fe and Co increases after annealing the FePt/FeCo/Si series. On the other hand, for FeCo/FePt/Si series, the intensity of L_3-edge of Fe decreases, while that of Co increases after annealing. This is due to the presence of vacant 3d-orbitals of Fe in the C_As, which gets occupied after annealing; and the creation of vacant 3d-orbitals in Co after annealing. From the above discussion it is apprehensive that there is charge redistribution between Fe and Co after annealing. And the process of charge transfer takes place differently in both the series i.e. the charge transfer greatly depends on whether the growth of FeCo is over Si substrate or over polycrystalline FePt thin film. Since the intensity of absorption peak of Fe decreases while Co increases after annealing series FeCo/FePt/Si, it can be concluded that there is a charge transfer from Co to Fe ions. However, in series FePt/FeCo/Si, the intensity of absorption of both Fe and Co increases. This shows that the interfacial electronic structure of this series film (FePt on top) is different from those with FeCo on top. The charge transfer could be to Pt or O ions surrounding Fe. Hence, Pt L-edge spectroscopy was performed to further examine the electronic structures of these stacked bilayers.

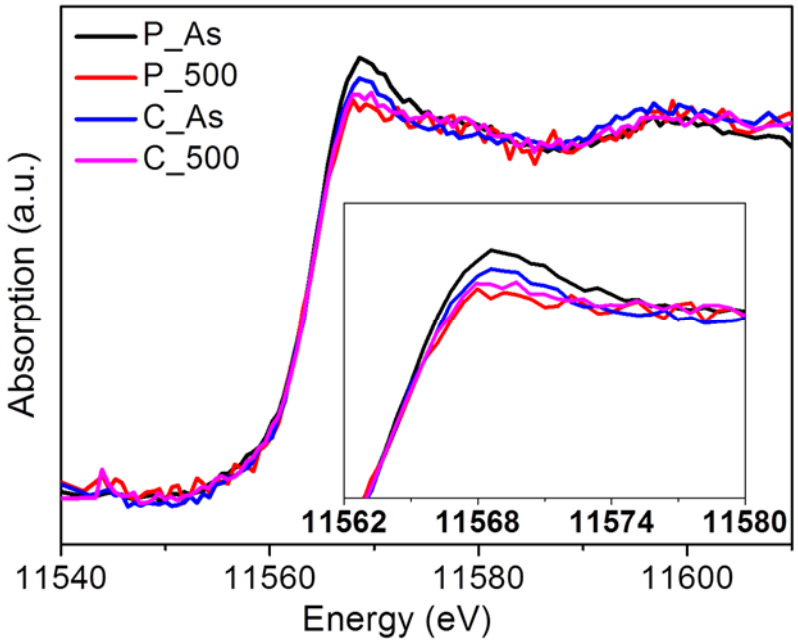

Figure 6. XAS spectra at Pt L_3-edge of FePt/FeCo/Si and FeCo/FePt/Si series. Inset shows an enlarged part of main edge peak region. Note that there is change in peak intensity implying charge transfer after annealing.

Figure 6 shows the L_3-edge of Pt for all the FeCo/FePt bilayers. The L-edge of Pt originates due to transition of electrons from 2p orbital to $5d_{3/2}$ and $5d_{5/2}$ bands [52]. It could be clearly observed from spectra that the intensity of absorption decreases after annealing both the series irrespective of the deposition of FePt over Si substrate or over polycrystalline FeCo. The decrease in the intensity of L_3-edge of Pt reveals reduction in the available empty 5d states, which could be ascribed to the hybridisation between Pt 5d and Fe 3d-4p electronic states [52]. Hence, it can be concluded that annealing affects the hybridization between the states of Fe and Pt. It can be noted that the intensities of both Fe and Co L_3-edges show an increase after annealing FePt/FeCo/Si series. This signifies that there is a considerable charge transfer both from Fe and Co to Pt after annealing FePt/FeCo/Si series. On the other hand, the intensity of Fe and Pt L_3-edge decreases, while Co L-edge increases after annealing in FeCo/FePt/Si, indicating the charge transfer from Fe to Co and Pt. These charge transfers between Co and Pt in FePt/FeCo/Si are possible only at the interface of two layers. Hence, it is clear that the modified interface between the two layers is responsible for the distinguished charge transfers in both the series. This interface between FeCo and FePt could be the possible reason for decrease in coercivity in the out of plane configuration in FePt/FeCo/Si series as compared to FeCo/FePt/Si.

Figure 7(a & b) displays the normalized XAS spectrum corresponding to Fe and Co K-edges for all the bilayered thin films. Along with the spectra of all the samples investigated in this report, Fe and Co K-edge spectra are also shown for their oxides viz. FeO, Fe_2O_3, Fe_3O_4, CoO, Co_2O_3 and Co_3O_4 as reference compounds. The spectra of Fe and Co K-edges constitute of two main parts: one is the main feature centred around 7130 eV and 7727 eV respectively for Fe and Co, and the other is the pre-edge feature centred around 7113 eV (for Fe) and 7710 eV (for Co). The former absorption edge occurs due to transition of electrons from Fe or Co 1s state to 4p empty states, while the latter defined pre-edge is a result of transition of electrons from 1s state to empty 3d orbitals. The transition from 1s to 3d state is dipole-forbidden, but it is quadrupole-allowed transition or allowed by transition of 1s electrons to the 3d-4p hybridized states.

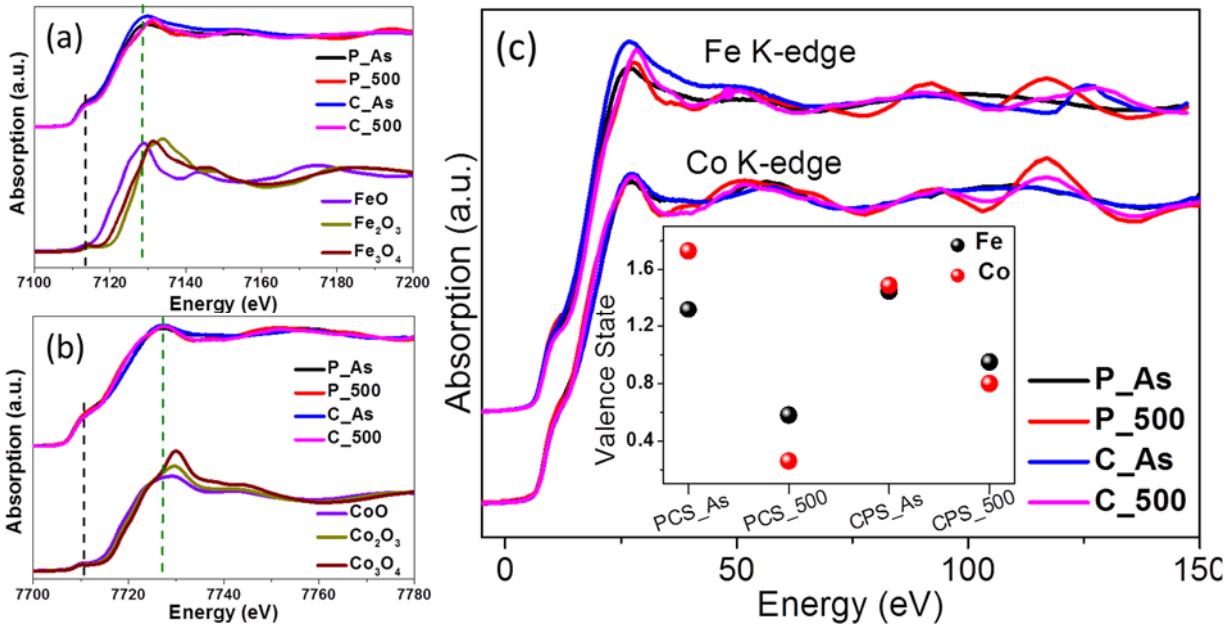

Figure 7. XANES spectra at absolute energy scale for (a) Fe K-edge (b) Co K-edge and (c) comparison of Fe and Co K-edge spectra in at relative energy scale.

Changes in the spectral shape of Fe and Co K-edge for all the samples with respect to all their oxides commonly known are appreciable and hence depict the electronic structure in the bilayered metallic films different from their oxides (shown in fig. 7(a) and (b)). The pre-edge features of metal Fe and Co shows a broad hump unlike a sharp peak observed in their corresponding oxides [48,53,54]. Similarly, the main absorption edge of Fe and Co metal appears rounded and rises with a gradual slope in contrast to the sharp increase in the main absorption edge for corresponding oxides [48,53,54]. The pre-edge and main absorption edge features observed in these bilayered samples are similar to the metallic Fe and Co foil

443 references reported in reference [48,54]. However, a relative variation in the spectral features
444 of all samples resulting due to unavoidable surface oxidation in the films and intermetallic
445 behaviour due to disordered structure cannot be neglected. The slope of main absorption edge
446 for annealed samples of both the series is smaller relative to the corresponding as prepared
447 samples, which results in the chemical shift of main absorption edge spectra towards higher
448 energy after annealing. Similar chemical shift in the main absorption peak of Fe K-edge for
449 FeCo and FePt alloys is attributed to the increased metallicity in the samples. This infers the
450 increase in metallic nature of FeCo/FePt films after annealing. The average valence of Fe and
451 Co estimated using corresponding first derivative K-edge spectra is shown as an inset of fig.
452 7(c). In agreement with the L-edge analysis, it can be seen that the average valence of Fe and
453 Co decreases i.e. the metallic character in the films increases after annealing.
454 In order to observe the local coordination environment around Fe and Co in all the samples,
455 the Fe and Co K-edge spectra in a relative energy scale is shown in fig. 7(c). Both the Fe and
456 Co K-edge absorption spectra are plotted with a relative scale of energy on x-axis. It can be
457 witnessed that the oscillations in the spectra at both Co and Fe K-edge differ before and after
458 annealing, suggesting that the local coordination environment around Fe as well as Co varies
459 with annealing. The as prepared samples of both series show suppressed oscillations as
460 compared to the corresponding annealed ones. This implies an increase in the metallic
461 content in bulk after annealing; since it is known that the oxides show reduced oscillations as
462 compared to their corresponding metals [54]. Perhaps, the variation in the local surroundings
463 after annealing both the series could be the consequence of enhanced crystallinity as evident
464 from the synchrotron XRD studies. Similar oscillations at Fe and Co absorption edges
465 indicate that Co is present in the system only as BCC phase of FeCo. Furthermore, the local
466 surroundings around Fe site are different in both the series annealed at 500 ˚C; since the local
467 surroundings of Fe involve Pt, Co as well as O in fcc, bcc and fcc structure respectively.
468 Hence, the XAS spectra for Fe, Co and Pt absorption edges show variations in the electronic
469 structure of the individual elements in FeCo/FePt bilayers before and after annealing. The
470 distinct charge transfer is observed at Fe, Co and Pt sites in the two cases when FePt is
471 deposited over Si substrate or over FeCo thin film.

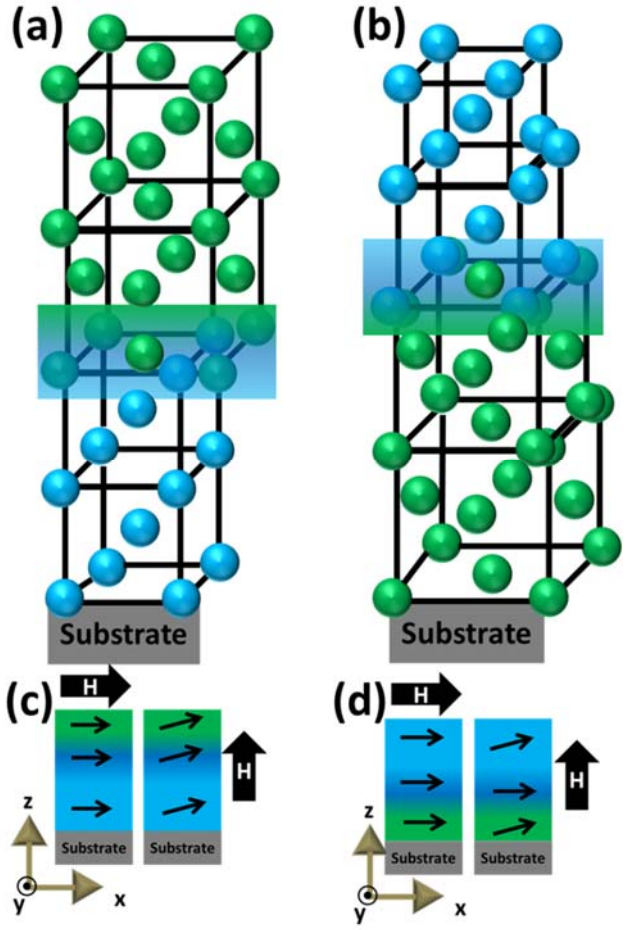

Figure 8. Schematic summarizing the comparison of structural parameters in (a) FePt/FeCo/Si and (b) FeCo/FePt/Si series where the blue spheres represent FeCo lattice and the green spheres represent FePt lattice and the corresponding pinning mechanism in (c) and (d) respectively.

Based on the aforementioned observations, a schematic for visualizing the impact of reverse stack order of FeCo/FePt bilayers on Si substrate is depicted in fig. 8. Probing the structural parameters through the interface reveals larger lattice misfit at the interface of FePt and FeCo in FePt/FeCo/Si series (fig. 8(a)) compared to the other series (fig. 8(b)). Such an interface leads to domain wall propagation mediated by pinning mechanism described in fig. 8(c) and 8(d). The arrows represent direction of average magnetization while applying the field H along x (inplane) and z (outplane) directions. The series with lesser lattice misfit at the interface i.e. FeCo/FePt/Si series shows large rise in outplane coercivity. Strong coupling in the outplane hysteresis of FePt/FeCo/Si_500 ensures coherent flipping of spins at the FeCo and FePt layers along with the interface. Despite the pinning behaviour observed in both the series after thermal annealing, the two-step hysteresis loop in FeCo/FePt/Si series can be explained by uncoupled magnetic phases possessing additional out-plane anisotropy. The ground state electronic configurations provide an evidence for the electronic charge transfer from Fe and Co to Pt after annealing FePt/FeCo/Si. On the other hand for FeCo/FePt/Si, there

are no electron interactions between Co-Pt, while strong interactions between Fe-Pt and Fe-Co after annealing were observed. The difference in oscillations at Fe and Co K-edge of the two series after annealing suggests that the local coordination geometry around the Co site is similar but Fe sites are different in both the series. This ensures the varied crystalline environment of FePt in the two series, indicated by gradient in the lattice parameter of FePt close to the interface in FeCo/FePt/Si_500 evident from fig. 1(c). Therefore, it can be inferred that the magnetic properties of the exchange spring FePt/FeCo system significantly depends on the order of individual layers deposited on substrate.

Conclusions

The structural, magnetic and electronic structure properties of FeCo/FePt exchange spring system prominently depend on the interfacial interactions between the two layers. The layered structure of FeCo and FePt examined using glancing angle dependent diffraction studies reveal that lattice parameters of FePt and FeCo at the interface remains the same as in bulk for FePt/FeCo/Si_500. While for the FeCo/FePt/Si_500, a strained interface is observed with expanded unit cell of FeCo and lesser lattice parameter of FePt at the interface as compared to the bulk. The increase in crystallite size of FePt after annealing is less for FePt/FeCo/Si series as compared to the other, which depicts that FeCo inhibits the crystalline growth of FePt. The in-plane M-H loops demonstrate a soft ferromagnetic behaviour in all bilayered samples, while the outplane M-H loops shows two-step magnetization reversal with high coercivity. The rise in coercivity for outplane configuration is attributed to the pinning dominated domain wall propagation. The out of plane magnetization of FePt is established in FeCo/FePt/Si series using FMR and outplane M-H curves measurements. The Fe, Co and Pt L-edge measurement indicates the electronic interactions between Fe-Co and Co-Pt after annealing FePt/FeCo/Si. While for FeCo/FePt/Si, the electronic interactions are prominent for Fe-Pt and Fe-Co. In addition, the oscillations at the far edge of Fe and Co K-edge reveal similar local coordination of Co in both the series, but differing local surroundings of Fe ascribed to the dissimilar crystallinity of FePt in FePt/FeCo/Si and FeCo/FePt/Si series.

Acknowledgements

The authors would like to acknowledge MCX Beamline, Elletra for providing us synchrotron XRD facilities through proposal number 20185163, and ICTP for financially supporting during the measurements. We gratefully acknowledge the project entitled “Magneto -Optic and Magnetic Multilayers” (EMR/2016002437 dated 14.03.2017), Department of Physics and Astrophysics, University of Delhi planned by SERB-DST. Author GV is also thankful towards Council of Scientific and Industrial Research (CSIR) for providing financial assistance in the form of fellowship. CLD, KA, SA and GV would also like to acknowledge the project number MoST 107-2112-M-032-004-MY3 and Taiwan Experience Education Program.

References

1. Bodnarchuk MI, Kovalenko MV, Pichler S, Fritz-Popovski G, Hesser G, Heiss W. Large-area ordered superlattices from magnetic Wustite/cobalt ferrite core/shell nanocrystals by doctor blade casting. ACS nano. 2010 Jan 26;4(1):423-31.
2. Salaheldeen M, Vega V, Ibabe A, Jaafar M, Asenjo A, Fernandez A, Prida VM. Tailoring of perpendicular magnetic anisotropy in Dy13Fe87 thin films with hexagonal antidot lattice nanostructure. Nanomaterials. 2018 Apr;8(4):227.
3. Prida VM, Salaheldeen M, Pfitzer G, Hidalgo A, Vega V, González S, Teixeira JM, Fernández A, Hernando B. Template Assisted Deposition of Ferromagnetic Nanostructures: from Antidot Thin Films to Multisegmented Nanowires. Acta Physica Polonica, A.. 2017 Apr 1;131(4).
4. Gelbrich T, Feyen M, Schmidt AM. Magnetic thermoresponsive core− shell nanoparticles. Macromolecules. 2006 May 2;39(9):3469-72.
5. Yuan T, Song X, Zhou X, Jia W, Musa M, Wang J, Ma T. Role of primary Zr-rich particles on microstructure and magnetic properties of 2: 17-type Sm-Co-Fe-Cu-Zr permanent magnets. Journal of Materials Science & Technology. 2020 May 6 (15): 73-81.
6. Chin TS. Permanent magnet films for applications in microelectromechanical systems. Journal of Magnetism and Magnetic Materials. 2000 Feb 1;209(1-3):75-9.
7. Süss D. Multilayer exchange spring media for magnetic recording. Applied Physics Letters. 2006 Sep 11;89(11):113105.
8. Williams EW. Magnetic thin films and multilayers in data storage applications. Mater. Des. 1992;13:115.
9. Kryder MH. Magnetic thin films for data storage. Thin solid films. 1992 Aug 28;216(1):174-80.
10. Kasatkin SI, Murav'ev AM, Vasil'eva NP, Lopatin VV, Popadinets FF, Svatkov AV. Thin-film multilayer magnetic sensors based on the anisotropic magnetoresistive effect. Russian Microelectronics. 2000 Mar 1;29(2):137-46.
11. Fujimori H, Ohnuma S, Kobayashi N, Masumoto T. Spintronics in metal–insulator nanogranular magnetic thin films. Journal of magnetism and magnetic materials. 2006 Sep 1;304(1):32-5.
12. Chen Z, Li S, Lai T. Laser-induced transient strengthening of coupling in L10-FePt/FeNi exchange-spring film. Journal of Physics D: Applied Physics. 2015 Mar 18;48(14):145002.
13. Liu L, Sheng W, Bai J, Cao J, Lou Y, Wang Y, Wei F, Lu J. Magnetic properties and magnetization reversal process of L10 FePt/Fe bilayers magnetic thin films. Applied surface science. 2012 Aug 1;258(20):8124-7.
14. Goyal R, Arora N, Kapoor A, Lamba S, Annapoorni S. Exchange hardening in FePt/Fe3Pt dual exchange spring magnet: Monte Carlo modeling. Journal of Alloys and Compounds. 2017 Feb 25;695:1014-9.
15. Wang B, Oomiya H, Arakawa A, Hasegawa T, Ishio S. Perpendicular magnetic anisotropy and magnetization of L 10 FePt/FeCo bilayer films. Journal of Applied Physics. 2014 Apr 7;115(13):133908.
16. Ma D, Wang Y, Li Y, Umetsu RY, Ou S, Yubuta K, Zhang W. Structure and properties of nanoporous FePt fabricated by dealloying a melt-spun Fe60Pt20B20 alloy and subsequent annealing. Journal of Materials Science & Technology. 2020 Jan 1;36:128-33.
17. Liu Y, Jiang Y, Zhang X, Wang Y, Zhang Y, Liu H, Zhai H, Liu Y, Yang J, Yan Y. Effects of annealing temperature on the structure and magnetic properties of the L10-FePt nanoparticles synthesized by the modified sol–gel method. Powder technology. 2013 May 1;239:217-22.
18. Toney MF, Lee WY, Hedstrom JA, Kellock A. Thickness and growth temperature dependence of structure and magnetism in FePt thin films. Journal of Applied Physics. 2003 Jun 15;93(12):9902-7.
19. Zha CL, He SH, Ma B, Zhang ZZ, Gan FX, Jin QY. Dependence of ordering kinetics of FePt thin films on different substrates. IEEE transactions on magnetics. 2008 Dec 16;44(11):3539-42.
20. Xu XH, Wu HS, Wang F, Li XL. The effect of Ag and Cu underlayer on the L10 ordering FePt thin films. Applied surface science. 2004 Jun 30;233(1-4):1-4.
21. Shen CY, Chang HW, Yuan FT, Lin MC, Su CC, Yeh HH, Huang MF, Wang CR, Shih CW, Chang WC. Energy product enhancement of FePt films by underlayering with Ti, Zr, and Hf. Applied surface science. 2014 Sep 15;313:755-61.
22. Ludwig A, Zotov N, Savan A, Groudeva-Zotova S. Investigation of hard magnetic properties in the Fe–Pt system by combinatorial deposition of thin film multilayer libraries. Applied surface science. 2006 Jan 31;252(7):2518-23.

23. Hsiao SN, Chou CL, Liu SH, Chen SK. Influence of pressure on (0 0 1)-preferred orientation and in-plane residual stress in rapidly annealed FePt thin films. Applied Surface Science. 2020 Apr 15;509:145304.
24. Xu XH, Li XL, Wang F, Jiang FX, Wu HS. A study of the effect of ZrO2 on the magnetic properties of FePt/ZrO2 multilayer. Applied surface science. 2006 Feb 15;252(8):2910-4.
25. Schmidt NY, Laureti S, Radu F, Ryll H, Luo C, d'Acapito F, Tripathi S, Goering E, Weller D, Albrecht M. Structural and magnetic properties of FePt-Tb alloy thin films. Physical Review B. 2019 Aug 28;100(6):064428.
26. Wei DH, Yao YD. Enhanced magnetic properties in FePt (001) epitaxial thin films by Cu capping layer. In2010 3rd International Nanoelectronics Conference (INEC) 2010 Jan 3 (pp. 704-705). IEEE.
27. Zhang J, Liu Y, Wang F, Zhang J, Zhang R, Wang Z, Xu X. Design and micromagnetic simulation of the L 10-FePt/Fe multilayer graded film. Journal of Applied Physics. 2012 Apr 1;111(7):073910.
28. Gu Y, Zhang D, Zhan X, Ji Z, Zhang Y. Structural and magnetic properties of RF sputtered FePt/Fe multilayers. Journal of magnetism and magnetic materials. 2006 Feb 1;297(1):7-16.
29. Goll D, Breitling A, Gu L, Van Aken PA, Sigle W. Experimental realization of graded L 1 0-FePt/Fe composite media with perpendicular magnetization. Journal of Applied Physics. 2008 Oct 15;104(8):083903.
30. Giannopoulos G, Reichel L, Markou A, Panagiotopoulos I, Psycharis V, Damm C, Fähler S, Khan I, Hong J, Niarchos D. Optimization of L10 FePt/Fe45Co55 thin films for rare earth free permanent magnet applications. Journal of Applied Physics. 2015 Jun 14;117(22):223909.
31. Vashisht G, Goyal R, Bala M, Ojha S, Annapoorni S. Studies of Exchange Coupling in FeCo/L1 0-FePt Bilayer Thin Films. IEEE Transactions on Magnetics. 2018 Nov 6;55(3):1-5.
32. X. Liua, and A. Morisako, “Soft magnetic properties of FeCo films with high saturation magnetization”, *J. Appl. Phys*., vol. 103, pp. 7E726-1-3, (2008).
33. Vashisht G, Kumar V, Bala M, Hussain Z, Reddy VR, Lamba S, Annapoorni S. Domain observation in electrochemically deposited FeCo nano-rods by MOKE microscopy and micromagnetics. Journal of Magnetism and Magnetic Materials. 2020 Mar 1;497:166064.
34. Guan XW, Cheng XM, Huang T, Miao XS. Interface structure and magnetism of CoFe/A1-FePt films with perpendicular magnetic anisotropy. Journal of Applied Physics. 2014 Dec 7;116(21):213910.
35. L. Rebuffi, JR Plaisier, M. Abdellatief, A. Lausi, P. Scardi, MCX: a Synchrotron Radiation Beamline for X-ray Diffraction Line Profile Analysis, Zeitschrift fur Anorganische und AllgemeineChemie640 (2014) 3100.
36. Minh PT, Thuy NP, Chan NT. Thickness dependence of the phase transformation in FePt alloy thin films. Journal of magnetism and magnetic materials. 2004 Jun 1;277(1-2):187-91.
37. Salaheldeen M, Martínez-Goyeneche L, Álvarez-Alonso P, Fernández A. Enhancement the perpendicular magnetic anisotropy of nanopatterned hard/soft bilayer magnetic antidot arrays for spintronic application. Nanotechnology. 2020 Sep 17;31(48):485708.
38. Kumar L, Kar M. Influence of Al3+ ion concentration on the crystal structure and magnetic anisotropy of nanocrystalline spinel cobalt ferrite. Journal of Magnetism and Magnetic Materials. 2011 Aug 1;323(15):2042-8.
39. Zhao ZL, Ding J, Chen JS, Wang JP. The effects of pinning layer on the magnetic properties of FePt perpendicular media. Journal of magnetism and magnetic materials. 2004 May 1;272:2186-8.
40. Bance S, Oezelt H, Schrefl T, Ciuta G, Dempsey NM, Givord D, Winklhofer M, Hrkac G, Zimanyi G, Gutfleisch O, Woodcock TG. Influence of defect thickness on the angular dependence of coercivity in rare-earth permanent magnets. Applied Physics Letters. 2014 May 5;104(18):182408.
41. Sharma P, Zhang Y, Makino A. Magnetic properties of L1 0 FeNi phase developed through annealing of an amorphous alloy. IEEE Transactions on Magnetics. 2017 Jul 17;53(11):1-0.
42. Medwal R, Gupta S, Rawat RS, Subramanian A, Fukuma Y. Spin Pumping in Asymmetric Fe50Pt50/Cu/Fe20Ni80 Trilayer Structure. physica status solidi (RRL)–Rapid Research Letters. 2019 Oct;13(10):1900267.
43. Talagala P, Fodor PS, Haddad D, Naik R, Wenger LE, Vaishnava PP, Naik VM. Determination of magnetic exchange stiffness and surface anisotropy constants in epitaxial ni 1− x co x (001) films. Physical Review B. 2002 Oct 31;66(14):144426.

44. Wu S, Abe K, Nakano T, Mewes T, Mewes C, Mankey GJ, Suzuki T. Thickness dependence of dynamic magnetic properties of soft (FeCo)-Si alloy thin films. Physical Review B. 2019 Apr 19;99(14):144416.
45. Von Der Heyden BP, Roychoudhury AN, Tyliszczak T, Myneni SC. Investigating nanoscale mineral compositions: Iron L 3-edge spectroscopic evaluation of iron oxide and oxy-hydroxide coordination. American Mineralogist. 2017 Mar 1;102(3):674-85.
46. Piamonteze C, Miedema P, De Groot FM. Accuracy of the spin sum rule in XMCD for the transition-metal L edges from manganese to copper. Physical Review B. 2009 Nov 10;80(18):184410.
47. Drozd V, Liu GQ, Liu RS, Kuo HT, Shen CH, Shy DS, Xing XK. Synthesis, electrochemical properties, and characterization of LiFePO4/C composite by a two-source method. Journal of Alloys and Compounds. 2009 Nov 13;487(1-2):58-63.
48. Kumar H, Ghosh S, Srivastava P, Kabiraj D, Avasthi DK, Olivi L, Aquilanti G. Stabilization of FeCo alloy phase in FeCo–SiO2 nanocomposites. Adv. Mat. Lett. 2013;4(6):390-7.
49. Lau JT, Rittmann J, Zamudio-Bayer V, Vogel M, Hirsch K, Klar P, Lofink F, Möller T, Issendorff BV. Size Dependence of L 2, 3 Branching Ratio and 2 p Core-Hole Screening in X-Ray Absorption of Metal Clusters. Physical review letters. 2008 Oct 7;101(15):153401.
50. Biesinger MC, Lau LW, Gerson AR, Smart RS. Resolving surface chemical states in XPS analysis of first row transition metals, oxides and hydroxides: Sc, Ti, V, Cu and Zn. Applied surface science. 2010 Nov 15;257(3):887-98.
51. Regan TJ, Ohldag H, Stamm C, Nolting F, Lüning J, Stöhr J, White RL. Chemical effects at metal/oxide interfaces studied by x-ray-absorption spectroscopy. Physical Review B. 2001 Nov 14;64(21):214422.
52. A. I. Figueroa, in Magnetic Nanoparticles. A Study by Synchrotron Radiation and RF Transverse Susceptibility, Springer Theses (Springer International Publishing, Switzerland), 2015.
53. Carta D, Mountjoy G, Gass M, Navarra G, Casula MF, Corrias A. Structural characterization study of FeCo alloy nanoparticles in a highly porous aerogel silica matrix. The Journal of chemical physics. 2007 Nov 28;127(20):204705.
54. De la Presa P, Rueda T, Hernando A, Ramallo-Lopez JM, Giovanetti LJ, Requejo FG. Spontaneous oxidation of disordered fcc FePt nanoparticles. Journal of Applied Physics. 2008 May 15;103(10):103909.